# Fatigue crack growth in IN718/316L multi-materials layered structures fabricated by laser powder bed fusion

**M-S Duval-Chaneac[1, 2], N Gao[1], R.H.U Khan[3], M Giles[1], K Georgilas[2], X Zhao[1], P.A.S Reed[1]**

[1] Materials Research Group, Faculty of Engineering and Physical Sciences, University of Southampton, Southampton, SO17 1BJ, UK

[2] NSIRC, TWI Ltd., Granta Park, Great Abington, Cambridge, CB21 6AL, UK

[3] TWI Ltd., Granta Park, Great Abington, Cambridge, CB21 6AL, UK

E-mail: marie-salome.duval-chaneac@affilliate.twi.co.uk or m-s.d.duval-chaneac@soton.ac.uk

## Abstract

Multi-materials additive manufacturing (MMAM) allows the functional optimisation of components by tailoring the addition of alloys at different design locations, in a single operation. The focus of this study is to investigate the ability to use additively manufactured multi-materials to control the near tip crack driving force, and mitigate crack propagation. Laser Powder Bed Fusion (L-PBF) technique was used to manufacture layered specimens combining IN718 and 316L materials, and tested to determine the effect of the different tensile properties of each alloy in the as-built (AB) state on the crack propagation process through multi-layer specimens.

The microstructure and fracture surfaces were studied using scanning electron microscopy (SEM). The mechanical properties of each alloy system were tested separately by tensile, micro and nanohardness testing. Fatigue crack growth tests were performed under three-point bending, then fractographically analysed. The effect of grain orientation in the transition in elasto-plastic response of dissimilar materials is detailed and linked to corresponding propagation rate fluctuations and the overall contribution to crack propagation rates.

## Key words

Multi-materials, additive manufacturing (AM), Interface, Fatigue analysis, Crack growth rate

# 1. Introduction

Multi-Materials Additive Manufacturing (MMAM) techniques allow the production of a new generation of components and the reduction of production cost, lead time, inventory and assembly [1] [2]. So far, multi-material parts have been predominantly made by using different types of joining techniques such as welding or brazing [3]. The joining of dissimilar materials inherently creates an interface, that can offer a gradient transition or a discrete interface, which locally affects the microstructure [4]. At the microstructural level, a number of defects can arise in the interface region during rapid solidification, such as intermetallic phase formation, distortions, porosities, residual stresses etc [5]. Whilst at the macroscopic level a gradient in mechanical properties is created, affecting the overall mechanical response of the component [6].

So far, Inconel 718 (IN718) and 316L austenitic stainless steel (316L) components produced as single-material AM have been extensively investigated [7][8][9][10]. For instance, IN718 is widely used in aircraft turbines, jet engines and steam turbines for power plants, due to its strength and corrosion resistance that can be maintained at elevated service temperatures up to 700°C. Whereas 316L is a well-known alloy, with good mechanical properties and excellent corrosion resistance, which can be found in infrastructure such as power plants, or pharmaceutical processing machinery. The combination of IN718 and 316L has been used in pressure tubes for nuclear fission reactors [8], [9], [11]. Both IN718 and 316L alloys possess a face centred cubic (FCC) crystal structure, and both alloys have similar coefficients of thermal expansion (CTE), of 13 μm/m.°C for IN718 and of 16 μm/m.°C for 316L, hence further supporting their ability to form a good cohesive interface, by reducing the residual strain caused by solidification shrinkage.

In addition to the intrinsic properties of each alloy, layers of materials having different elastic and plastic properties create a gradient in mechanical properties that directly affects the crack driving force and therefore plays an important role in determining the fatigue and fracture behaviour of multilayer components. A gradient in mechanical properties can find a use in a variety of engineering applications for multi-phase materials[12]. Composites or graded structures have been designed to use this property gradient to benefit the component response. Studies on the effect of a soft interlayer on crack propagation were conducted on aluminium and polymer layered systems, showing that the crack propagation was effectively shielded leading to crack arrest at the second interface (on transition from soft to hard material) [13].

However, the fatigue behaviour in components produced by AM techniques is relatively new due to the very specific microstructure and defects that can arise from the manufacturing technique [14]. The rapid cooling induced by AM affects the phase formation, grain structure, and the mechanical response of alloys fabricated in this way [15][16]. IN718 is a precipitation strengthened alloy that commonly requires thermal post-treatment to obtain the optimal precipitation of secondary strengthening phases. However IN718 produced by L-PBF is known to develop localised micro-segregation of heavier elements such as Nb and Mo surrounding sub-cells and grain boundaries with high density dislocations [17][18]. Additionally in the AB state IN718 does not undergo the appropriate precipitation of the main strengthening phases such as gamma prime ($\gamma'$) and gamma double prime ($\gamma''$), the alloy has not been exposed to the appropriate thermal post treatment, hence has not achieved its optimal strength. However 316L

produced by L-PBF in its AB state possesses high strength and good ductility [19][20]. High cycle fatigue (HCF) and long crack propagation behaviour of L-PBF 316L have been studied by other researchers, showing that the ductile response of 316L leads to good fatigue performance in the AB state [21][22] .

In this study, L-PBF multi-material layered 316L/IN718 specimens are investigated in their AB state to study the effect of the microstructure on mechanical properties and fatigue performance and to understand the underlying controlling mechanisms of crack propagation in MMAM layered structures.

## 2. Materials and Methods

Both 316L and IN718 alloy powders were gas atomised by Sandvik Osprey producing spherical metallic powder particles in the size range of 20-50 µm. The powder size was measured using Malvern Morphologi 4 automated microscope, flowability was measured by the Hall Flowmeter funnel (measuring the flow time for 50g of powder), and tap density was measured for 3000 taps, according to the ASTM B213 standards [23]. The chemical composition of the powder was measured by external contractor AMG analytical (UK) by Inductively Coupled Plasma (ICP), and for lighter elements such as Carbon and Oxygen, contents were measured by thermal infrared and inert gas fusion respectively (LECO).

The L-PBF process was conducted using a HUAKE PM250 machine under an argon gas protective atmosphere, using the parameters shown in Table 1. The scanning strategy chosen was island scanning with a size of 5mm, and the scanning direction of each layer was alternated through a 90° angle. The ratio of process parameters, also named as the energy density ratio ($E_{dv,}$ see in Edv=P⁄h × t × v⁄ $[J/mm^3]$ ), is often used for process parameter optimisation:

$$E_{dv} = \frac{P}{h \times t \times v} \ [J/mm^3] \quad (1)$$

where *P* is the power, *h* the hatch spacing, *t* the thickness of the powder layer displayed and *v* the scanning speed [24]. The energy density ratio employed for both materials was $E_{dv} = 139.9\ J/mm^3$, which is within the optimal range of process parameters for high densification of each material according to studies on process parameter optimisation [25][26].

Table 1: L-PBF Process parameters used in this study for both 316L and IN718

| Laser Power | Scanning speed | Hatch space | Layer thickness | Layer rotation |
|---|---|---|---|---|
| 300W | 900mm/s | 0.08mm | 0.03mm | 90deg |

Bend bar specimens for fatigue testing were manufactured with dimensions of 10x10x60 mm, with IN718 as the top layer and 316L as the bottom layer (10x5x60 mm dimensions for each layer, as shown in Figure 2). Six tensile rods of Ø10x60 mm dimensions were manufactured respectively for IN718 and 316L to test the tensile properties of each alloy separately. In order to assure consistency of grain orientation in the bending and tensile specimen, all the specimens were produced with their main longitudinal axis parallel to the building plate plane (Figure 2).

For metallographic analysis, bend bars were cut orthogonally to the longitudinal direction, then mounted in conductive Bakelite. Top surfaces of the specimens were mechanically ground using 800 and 1200 silicon carbide (SiC) grit papers before polishing using 6 µm, 3 µm , 1µm and 0.25 µm diamond finish. Etching was performed with: $H_2O$: HCl: $H_2O_2$ solution in 4:2:1 proportions. Porosity and microstructural observations were made using an Olympus BX-51 optical microscope (OM). ImageJ software was used on multiple micrographs, to quantify the porosity content of each specimen. For each specimen six micrographs were taken providing a total area of study of 54.6mm². Scanning electron microscope (SEM) and X-ray spectroscopy (EDS) analysis were conducted by JEOL-JSM 5910 under 15-20kV for SEI imaging, at a typical working distance between 8.5 to 10mm. Backscatter electron (BSE) imaging and electron back scatter diffraction (EBSD) analysis were conducted using 20kV and a 120 µm aperture, a step size of 0.57µm and Channel5-HKL software. The observations were conducted along the build orientation of the specimen (z direction), then analysed by using Aztec software for grain size, shape and orientation. Macro-observation of specimen fracture surfaces was carried out using an Alicona G4 Infinite Focus, to allow roughness imaging for the fracture surfaces.

Vickers micro-hardness (HV) tests were conducted in accordance with BS EN ISO 6507 [27]. Hardness was measured using 300gf with dwell time of 15s. Measurements were made on cross sections of the specimens (10mm of edge length), with 50µm distance between each indentations. Nano-indentation measurements were taken across the interface to assess the hardness and modulus changes, 50 indent rows offset by 30 µm were made, with 5 indents per row spaced by 10 µm each, for a total length of measurement covering 1500 µm across the interface region (750 µm in the Inconel layer and 750 µm in the 316L layer). Measurements were done in depth control until 300 nm depth, indentation speed was set at 7mN/s.

Tensile tests were carried out at room temperature by external contractor Westmoreland mechanical testing (UK), in accordance with ASTM E8 standard at room temperature [28]. An extensometer was used for the first part of the test at a strain rate of 0.005 mm/mm/min, then switching to cross head displacement at a strain rate of 0.05 mm/mm/min for a faster displacement rate until final failure.

Long crack tests were performed under three-point bending, on an Instron8502 servohydraulic machine, with sinusoidal loading at R = 0.1, and frequency f=10Hz. The bend bars were notched in the centre using wire cutting to produce single edge notched bend (SENB) samples as shown in Figure 1. The depth of the notch is 1.25mm, corresponding to 1/4 of the depth of the layer (or 1/8 of the total depth of the bend bar). The pre-cracking was carried out by load shedding from an initial ΔK (of 15 MPa√m), then successively stepped down by 10% increments, after the crack grew through 4 monotonic plastic zone sizes at a given ΔK-level (down to a ΔK of 10.4 MPa√m for 316L and 12.6 MPa√m for IN718). Subsequent crack growth tests were conducted following the BS EN ISO 12108:2012 standard [29] under constant load,

increasing ΔK-conditions. One test was performed under constant ΔK-conditions, by altering the loading condition as the crack advanced to keep ΔK within 10% of the original value, in order to determine the crack propagation rate base line within each layer for a given crack tip stress intensity factor (results are displayed in section 3.4). The top surface of the specimens was ground using 120, 800, 1200 SiC grit paper and then polished using 6 µm, 3 µm, 1 µm diamond suspension. Crack length was monitored by a direct current potential drop (DCPD) method. Two probes were welded on the top surface on each side of the initial notch (named X values) and the other two probes (named Y) were welded on the lateral side (away from the center) to measure the base line potential of the current flow in the specimen. The fatigue crack growth rates da/dN were then derived from the curve of the variation in the electrical potential with time, translated to an empirically determined crack length *a* versus *N* relationship, and *da/dN* determined by the secant method. A standard calibration using tin foil was carried out to ensure the correct $V/V_o$ to *a/W* relationship for the DCPD device. This technique was employed because the resistivity of both alloys were considered similar in regards to the specimen dimensions: 7.400E-07 Ohm-m for 316L and 1.250E-06 Ohm-m for IN718, hence effects on the calculation of crack length were considered negligible, this was also checked by post-test crack length measurements.

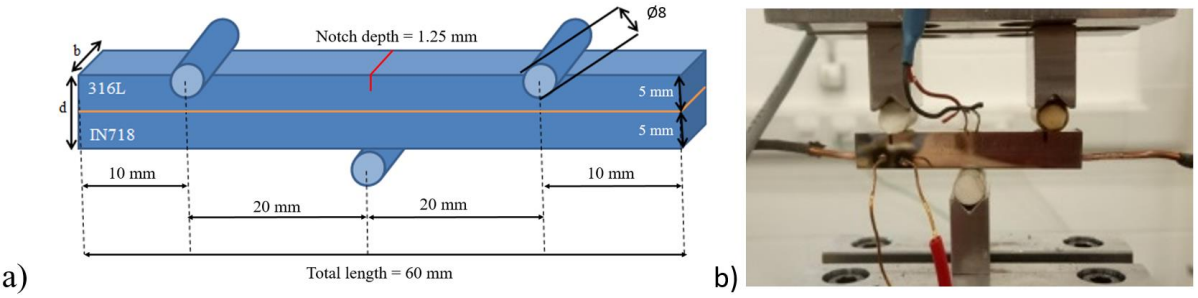


Figure 1: a) Schematic of notched bend bars under 3 point bending, b) Image of specimen including DCPD wire setting.

# 3. Results & Discussion

## 3.1. Characterisation of the metallic powders

The physical properties of the powders are displayed in Table 2 and the analysis of the elemental composition is displayed in

Table 3.

The 316L powder used in this study has more satellites and some agglomeration of powder creating a larger mean diameter, but also allowing a more compact tap density by interstitial powder stacking, which reduces the risk of creating porosities during the fabrication process. The chemical composition of 316L powder shows a long list of minimal elemental additions however, these concentrations remain very low. Similarly, the main chemical composition of

IN718 powder falls within the range of the standard alloy composition except with some minor elemental traces. However, it is important to note the presence of N in the composition of 316L. N solute atoms can lower the stacking fault energy of 316L SS and have an effect on deformation twining, supporting its good tensile ductility of L-PBF 316L [30].

Table 2: Physical powder properties

| | 316L | IN718 |
|---|---|---|
| Powder diameter size | 28.2±12 μm | 22.5±7 μm |
| Tap density | 5.4 g/cm³ | 6 g/cm³ |
| Flow ability | 15 ±0.3 g/s | 11.6±0.1 g/s |

Table 3 : Chemical composition of IN718 and 316L powders used in this study, and comparison with standard material

| Element (wt%) | 316L Powder | IN718 Powder | Standard wrought 316L | Standard wrought IN718 |
|---|---|---|---|---|
| Ni | 12.29 | 52.46 | 10 - 14 | 50 - 55 |
| Cr | 17.34 | 18.71 | 16 - 18 | 17 - 21 |
| Fe | 64.95 | 19.57 | Bal. | Bal. |
| Nb | 0.04 | 4.8 | - | 4.75 - 5.5 |
| Mo | 2.49 | 2.93 | 2-3 | 2.8 - 3.3 |
| Ti | <0.02 | 0.69 | - | 0.65 - 1.15 |
| Al | <0.02 | 0.36 | - | 0.2 - 0.8 |
| Cu | 0.17 | 0.02 | - | 0.3 max |
| C | 0.02 | 0.02 | - | 0.08 max |
| Co | 0.08 | 0.09 | - | 1 max |
| Mn | 1.49 | 0.04 | 2 | 0.35 max |
| Si | 0.85 | 0.09 | 0.75 | 0.35 max |
| B | <0.02 | <0.02 | - | 0.006 max |

### 3.2. Characterisation of the microstructure

Figure 2 b) shows the L-PBF IN718/316L layered structure in the AB specimen microstructure viewed on the YZ plane. IN718 has solidified directionally forming columnar dendritic grains with a cellular sub-structure across multiple layers, while an equiaxed cellular sub-structure was observed in 316L. These are delimited by the meltpool shape and abruptly change in growth direction from one melt track to the next (Figure 3 a) [31]. Equiaxed cells grow from the external boundary of the melt pool towards the centre, aligning with the heat flux direction [32]. Sub-cells are observed within the range of 0.5 to 1μm in diameter for both 316L and IN718, which is consistent with values from the literature for similar material [20] .

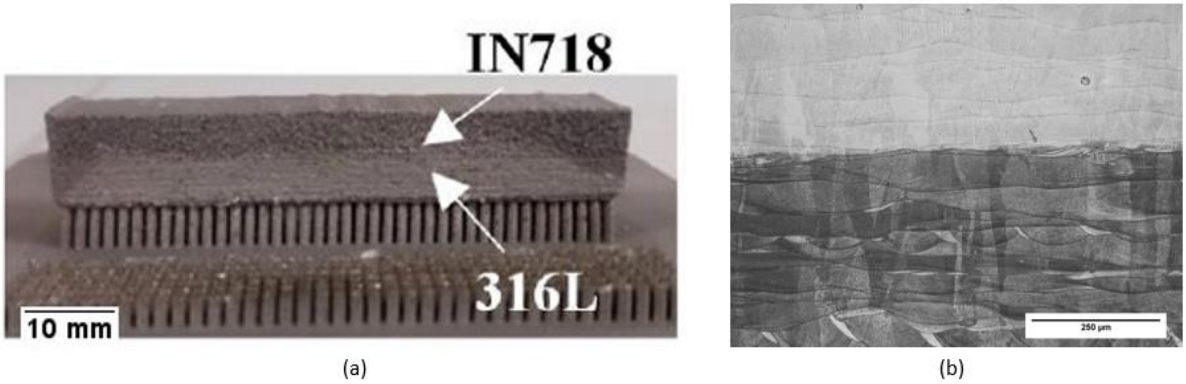


Figure 2: a) Image of bend bar specimen building orientation on base plate, b) Polished and etched cross section of the interface.

The AB microstructure reveals the presence of processing defects: some lack of fusion pores were observed in the IN718 layer, while small cracks due to liquation cracking are observed at the dissimilar materials interface (Figure 3 b). Liquation cracking can be found in rapidly solidified alloys with high alloying contents, which widen the solidification temperature range. Liquation cracking occurs in the remaining partially melted zones, surrounding the primary solidified grains and usually forming cracks along grains or sub-grain boundaries [33] [34].

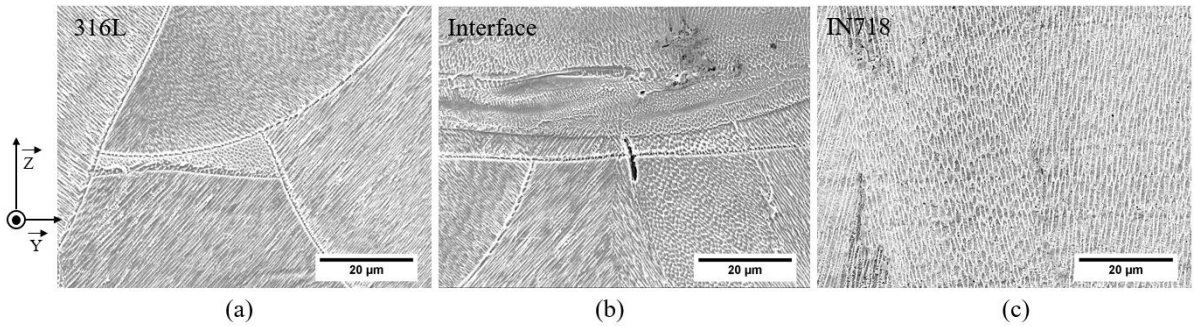


Figure 3: SEM view of polished and etched specimen, a) 316L layer, b) at the interface, c) IN718 layer

Figure 4 shows a grain orientation map across the bi-material interface. The columnar texture in the <001> direction is visible in both materials, which is expected for a face centred cubic (FCC) crystal structure when the building orientation (following the z-axis) is aligned with a favourable grain growth for the crystal structure. Because both 316L and IN718 alloy matrices are FCC, some grains show coherent growth across the interface. No major defects were observed at the interface, except for the sporadic liquation cracking. Figure 5 shows the percentage distribution of grains by size range and the associated aspect ratio in both IN718 and 316L layers. It shows that smaller grains (≤5µm) tend to be rounder than large grains (30-40µm diameter). This is due to the directional solidification of larger columnar grains oriented in the thermal gradient direction (following the build orientation along the z-axis direction). Over 50% of the total grains are below 5µm diameter for both alloys, and the smaller grains are formed around the columnar grains due to partial remelting and adjacent meltpool overlap. It can also be observed that IN718 grains have high aspect ratio that correspond to the SEM observation of the strong columnar texture in the <001> building orientation, while the 316L

grains possess a rounder shape due to the more equiaxed solidification they appear to have experienced.

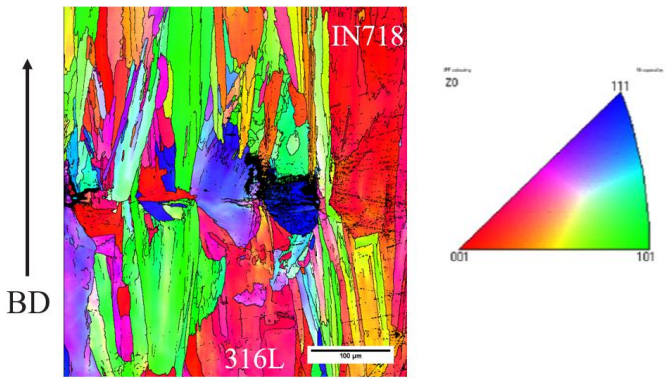


Figure 4: EBSD grain orientation map of the interface with IN718 at the top and 316L at the bottom

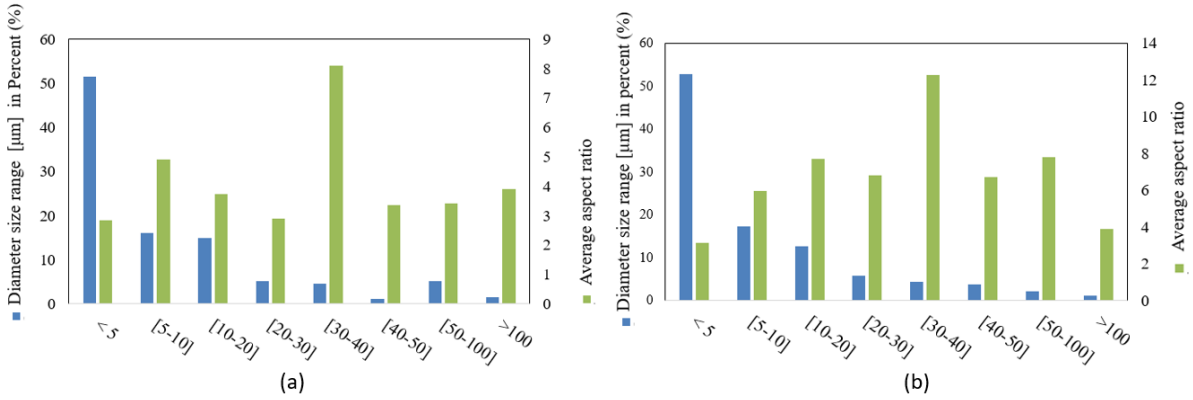


Figure 5: Grains size range percentage and aspect ratio: a) within the 316L layer, b) within IN718 layer

### 3.3. Hardness and tensile properties

Vickers micro hardness was measured on the cross section of the bilayer specimen, as shown in Figure 6. It can been seen that an average of 237 Hv and 290 Hv is obtained for the 316L and the IN718 layers respectively, both values are consistent with studies on similar materials processed by L-PBF in AB state [35], [36].

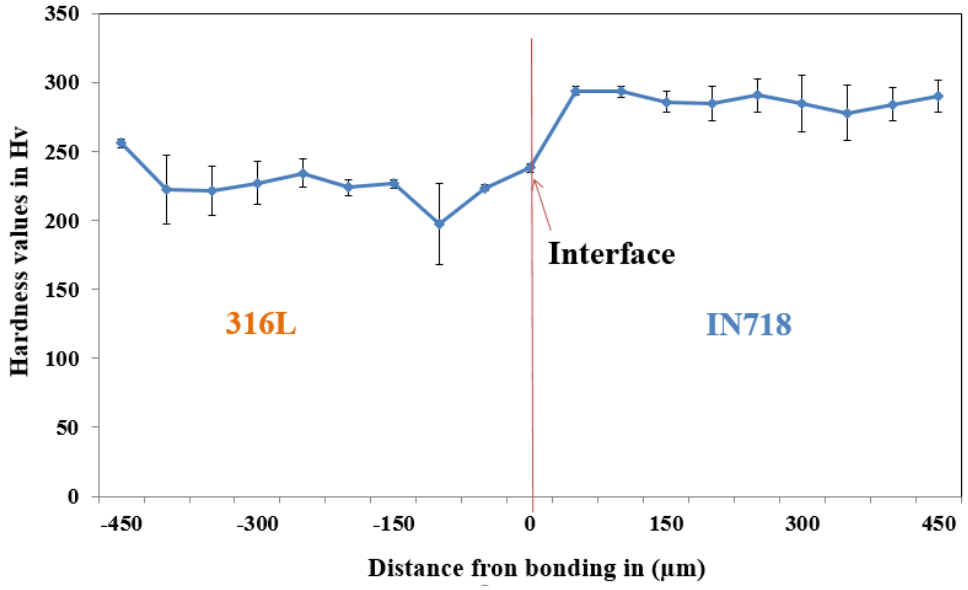


Figure 6: Vickers micro-hardness measured on the cross section of the specimen

Nano indentation was used to perform a more detailed analysis of the nano-hardness and reduced modulus variation across the interface. A map was created by averaging all the data points, and the results are displayed in Figure 7. The hardness transition at the interface shows an average value of 250Hv by micro-hardness measurement, while nano-indentation mapping shows a clear transition between each layer without showing any local loss of properties. The reduced modulus presents a more continuous transition from IN718 to 316L because the elastic properties of both materials is more dependent on the close-packed nature of the FCC crystal structure and similar bonding strengths for the transition metal alloys. The overall reduced modulus is 156 ± 58 GPa for 316L and 164 ± 15 GPa for IN718, these are somewhat less in comparison to the values typically reported in the literature, ie ~200GPa [37].

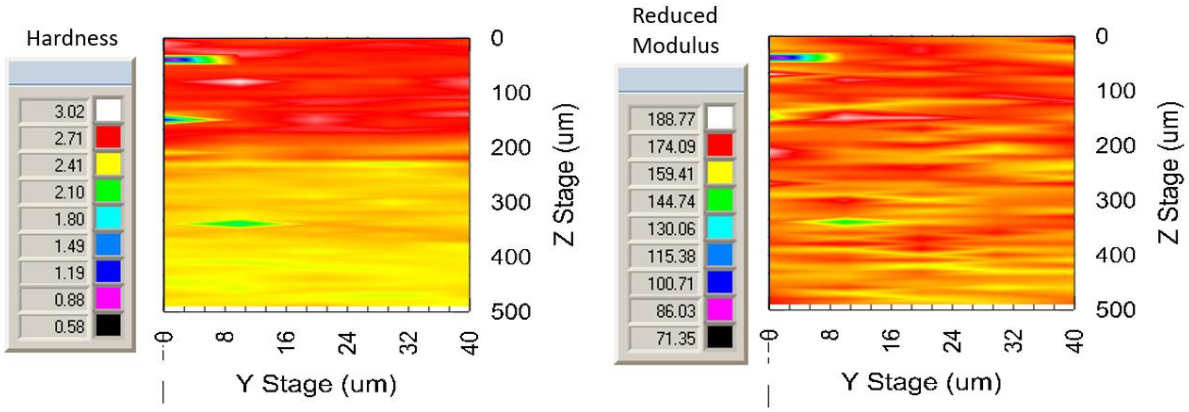


Figure 7: Scaled maps of nano indentation measurements at the interface between 316L (lower layer) and IN718 (upper layer), a) Nano-hardness, b) Reduced modulus

The tensile properties of each alloy were tested separately by static tension testing, and the results are displayed in Table 4, a comparative figure is also displayed in the Figure 8.

Table 4: Mechanical properties of each material from tensile tests and * nanohardness test

| | E (GPa)* | $\sigma_y$ (MPa) | $\sigma_u$ (MPa) | Hardness (GPa)* |
|---|---|---|---|---|
| 316L | 156 ± 2 | 588 ± 2 | 709 ± 3 | 2.1 ±0.04 |
| IN718 | 165 ± 2 | 677 ± 11 | 784 ± 55 | 2.7 ±0.3 |

As shown in Tab. 4, the elastic properties of both alloys are more or less similar, which was expected considering that both alloys share the same FCC crystal structure. However, the yield strength ($\sigma_y$) and the ultimate tensile strength ($\sigma_u$) show some difference. Compared to wrought 316L the properties of L-PBF 316L are higher [38]. Whereas AB-IN718 doesn't meet the static tensile properties defined by standards [39].

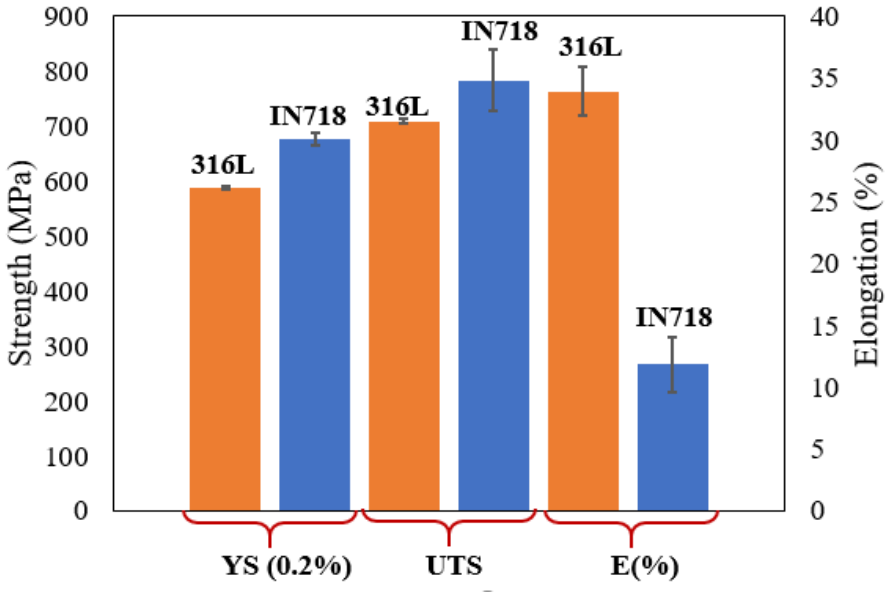


Figure 8: Comparison of 316L and IN718 static tensile properties

Additionally the overall ductility achieved in both alloys shows a greater difference, as displayed in Figure 9. The % elongation of the 316L alloy fabricated by L-PBF in AB condition is remarkable, and this mechanical response has been reported extensively elsewhere in the scientific literature [19]. Under severe plastic deformation when the necking of the specimen takes place, the triaxial stress state activates more shearing and allows twinning induced plasticity to occur within the crystal structure, causing the remarkable elongation and ductility of L-PBF 316L in the AB condition [30], [40] [19]. The plastic response under deformation is relevant in contributing to the fatigue crack propagation response in multi-layer specimens.

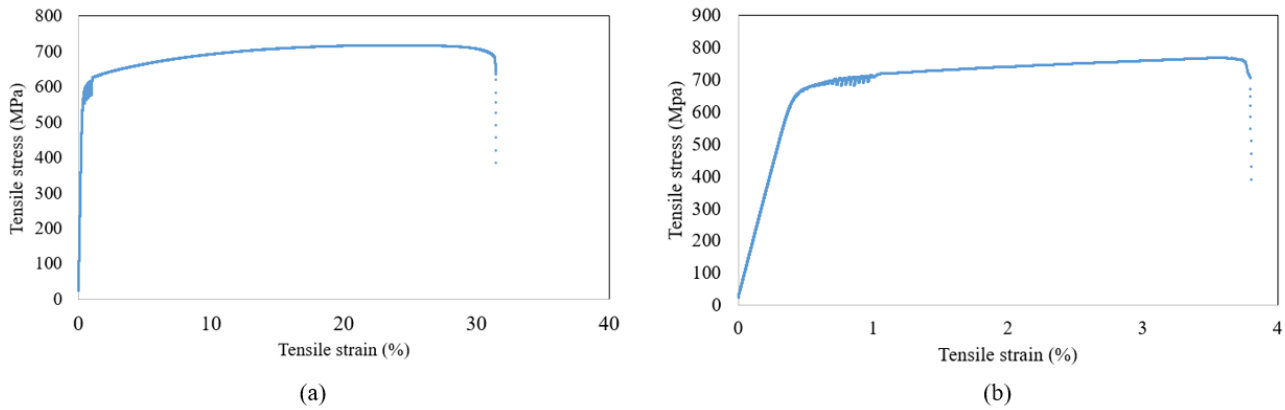


Figure 9: Stress strain curves obtained under displacement control loading for a) 316L material and b) IN718

## 3.4. Fatigue testing

Long crack fatigue propagation tests were performed in order to assess the crack propagation response of layered 316L/IN718 MMAM specimens. The crack growth configuration presented here is named the Crack Arrester (CA) configuration as the direction of the crack propagation is growing orthogonally through layers, in opposition to a Crack Divider (CD) configuration where a crack propagates through multiple layers at once [41].

The crack growth rate is a function of the local crack tip stress intensity factor range ΔK, and is displayed in Figure 10 for the two fatigue tests performed on the bi-layered specimens. For the first test specimen with the initiating notch located within the 316L layer, the crack propagates within the 316L layer (plotted in orange), and then crosses the interface and further grows toward the IN718 layer (plotted in blue), thus transitioning from soft-to-hard layer. For the second test specimen with a notch in the IN718 layer, the crack firstly initiates within the IN718 layer and propagates through the interface in a transition from hard-to-soft layer. The second test specimen that started crack growth within the IN718 layer (top curve), displays a Paris law growth curve that can be described by the following equation:

$$\frac{da}{dN} = 7 \times 10^{-7} \Delta K^{1.9} \qquad (2)$$

This description seems consistent with the results published for similar crack growth data for IN718 fabricated by L-PBF [42]. It appears that the softer 316L layer has not further increased the crack growth rate noticeably, although that could simply be due to the fact that crack growth rates were very high anyway at this point in the test.

When crack propagation gradually crosses a transition from a material with lower strength or stiffness (a more compliant layer, in our case 316L) towards a material with higher strength (a stronger layer in our case IN718), the gradient in mechanical properties induced by the dissimilar materials transition can directly affect the crack tip driving force. A shielding effect occurs when the stronger layer just ahead of the crack tip experience less deformation (that the softer/more compliant layer) for the same applied load, it is commonly considered that the stronger layer "carries the load", and hence decreases the local driving force at the crack tip

(embedded within the softer layer). Conversely when the transition occurs from a harder material towards a softer one the crack tip stress field undergoes an anti-shielding effect (more deformation occurs ahead of the crack tip), hence causing an acceleration in crack propagation rate. The bigger the difference between the materials properties, the more visible the effect of shielding and/or anti-shielding should be [6].

However, in the first crack growth test the crack that initiated from the 316L layer displayed a more scattered early growth rate behaviour and has reached a high enough ΔK that rapid failure ensued shortly after the crack crossed the interface. The increased crack growth scatter and local decreases in growth rate within the 316L layer are linked to the equiaxed nature of the solidified microstructure in 316L. The presence of grain boundaries and high angle boundaries surrounding the meltpools, are expected to form locally weaker zones with defects and enhanced localised deformation, hence causing preferential tortuous crack propagation. Such crack growth rate scatter was not observed in the 316L layer at higher values of stress intensity factor when the crack growth was initiated within the IN718 layer. The overall difference in roughness of the fracture surfaces are compared in Figure 14.

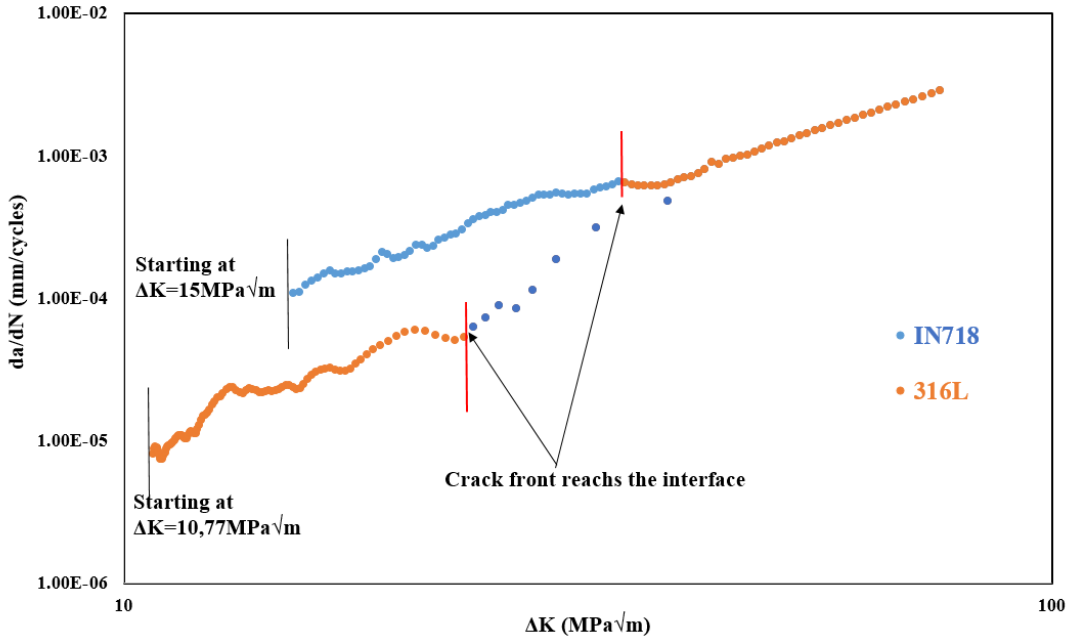


Figure 10: Crack growth rate (da/dN) versus the stress intensity factor range ΔK, propagation through bilayer specimen

The crack propagation under increasing ΔK conditions through the bi-layer specimen has showed that no significant effect of the dissimilar material interface such as shielding and anti-shielding was observable. However, at lower stress intensity factor values it was considered that the variation in grain structure and orientation may have a great impact on crack tortuosity and hence on propagation rate. This is further proven in the fractography analysis in section 3.5. It was observed that within the IN718 material the large elongated columnar grain structure, where the longest axis was parallel to the direction of the crack advance causes an apparently continuous growth rate. While the more equiaxed grain structure of the 316L material has caused more local crack slowing and tortuosity in the crack propagation at lower stress intensity levels as can be seen in the comparison of the overall fracture surfaces in Figure 14.

## 3.5. Fracture surface analysis

Fractography analysis of the crack propagation through the bi-layer specimen, initiating from the 316L (softer) layer is displayed in Figure 11. The overall fracture surface in the 316L region displays rough features. The observations show that tortuous intergranular crack path propagation has occurred along the equiaxed microstructure boundaries. At the lower part of the 316L layer (just before the interface), striations of the size ~1.6 μm can be seen, which are characteristic of crack propagation rates in the Paris regime. The crack propagation rate had reached 1μm/cycle at an already advanced propagation stage around a stress intensity factor range of 22-25MPa√m. Up to this point the tortuous intergranular crack path was more prevalent than Stage II crack growth evidenced by striation marks. This could then explain the scatter in the crack propagation rate at lower stress intensity factors in the early stages in the crack propagation. The importance of grain misorientation in crack propagation in AB L-PBF 316L material has also been observed by Riemer et al.[43] in their study on crack growth within 316L CT specimen. Melt pool boundaries and grain boundaries have lower bonding strength because they are preferential sites for segregation of defects, intermetallics or carbide formation. Hence, the melt pool boundaries and grain boundaries, which are also visible as high angle boundaries in the EBSD map, can be regarded as the weaker regions of the material [20].

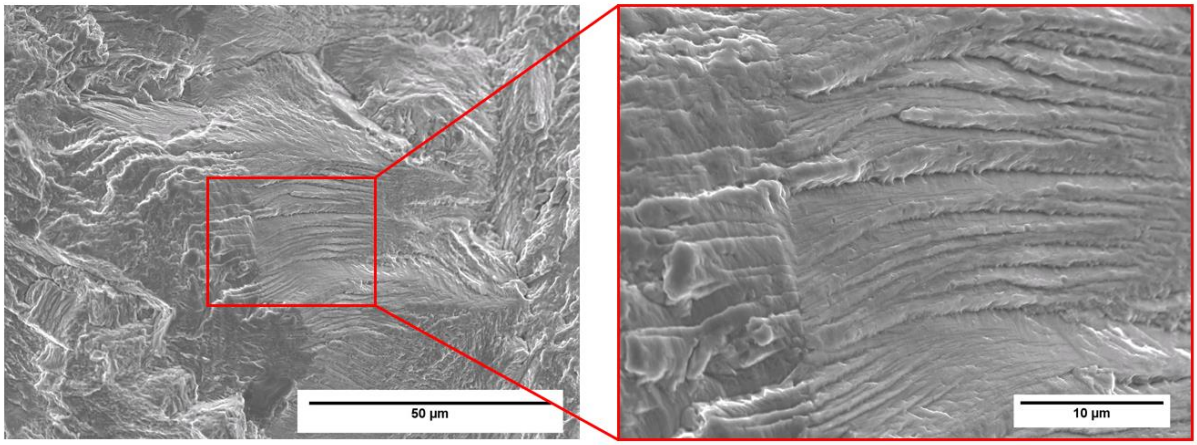


Figure 11: SEM fractography of 316L initiating layer

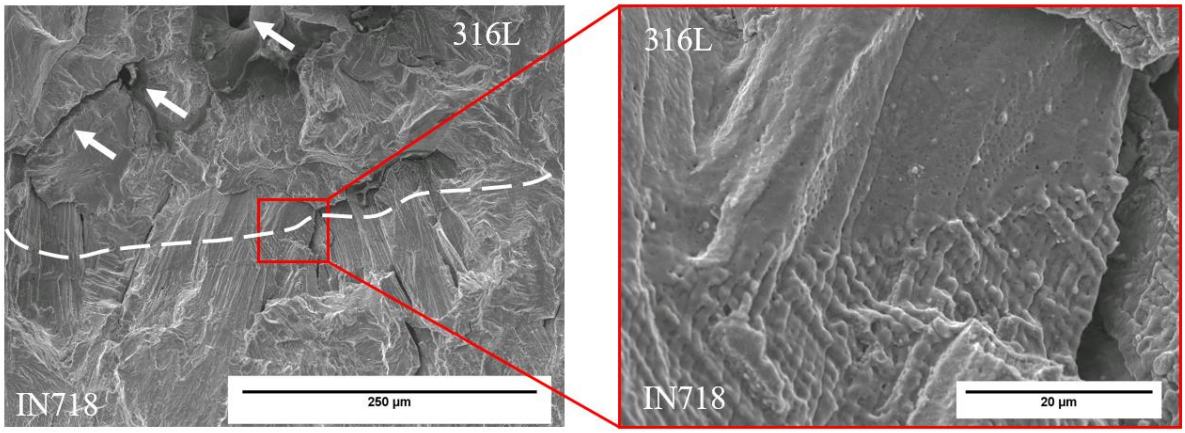


Figure 12: SEM fractography of the interface between the upper 316L layer and the IN718 bottom layer

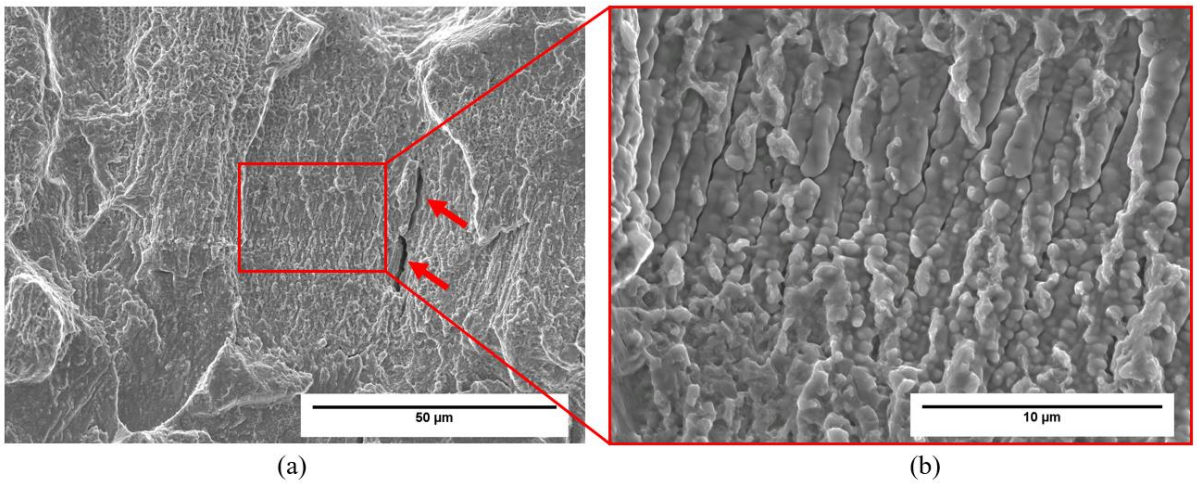


Figure 13: SEM Fractography of crack propagation in the IN718 bottom layer

Figure 12 a) shows small porosities (indicated by white arrows) and liquation cracking around the interface, supporting local secondary crack joining in the 316L. Figure 12 b) shows an enlarged view of the transition in the microstructure at the interface. It can be seen that IN718 and 316L SS do not display similar microstructural features, due to the difference in grain solidification. Dendritic solidification appears in the IN718 layer and the fracture surface shows clearly dendritic decohesive crack propagation in the IN718 layer as can be seen in Figure 13. Some liquation cracks are visible in between the columnar dendrites (indicated by red arrows), which seem not to have affected the crack propagation process much.

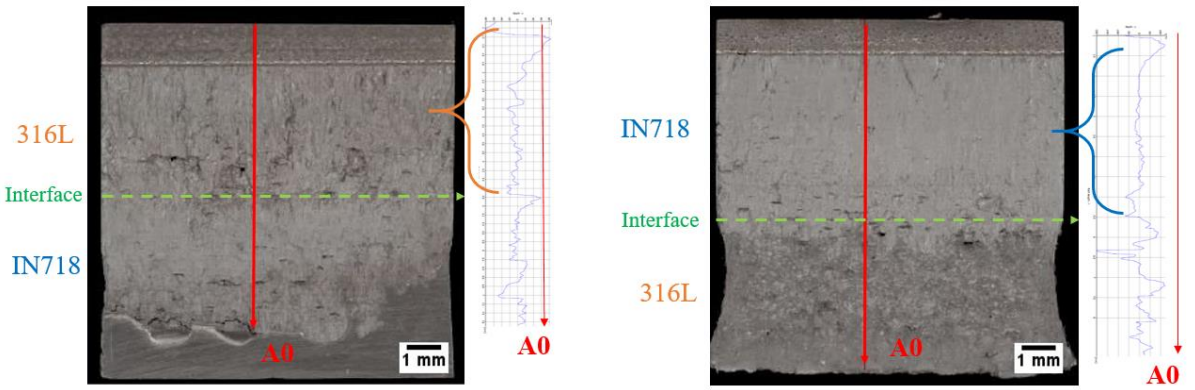

Figure 14: Alicona view of each fracture surface and roughness profile (named A0 on the right side of each surface), a) crack initiated from 316L layer, b) crack initiated from IN718 layer

Alicona has been used to quantify the roughness difference of the fracture surface of each specimen and the results are displayed in Figure 14 . It can be seen that 316L as the upper layer (shown in Fig. 14 (a)) displays a rougher profile than IN718 as the upper layer (shown in Fig. 14 (b)) within equivalent stress intensity factor ranges ($\Delta K$ was typically 12-20 MPa$\sqrt{m}$ within the upper layer). In the specimen where the crack started from the IN718 layer, a very flat and smooth surface was observed, mainly transgranular with no specific features. This is consistent with the obvious columnar dendrite microstructure of IN718 shown in Fig. 13 and the very smooth crack growth rate displayed in Figure 10. Because of the directional solidification of columnar dendrites and the associated crack path, the crack front has not deviated and propagation behaviour was not shielded by crack path tortuosity [43].

This fractography analysis reveals the impact of the grain structure on the crack propagation, and how the lower alignment of the equi-axed grains in the 316L has impacted the crack tortuosity, while the elongated and favourably aligned columnar grains of the IN718 layer tend to have facilitated the crack propagation path through the microstructure. Therefore, the impact of the dissimilar plastic properties transitioning at the interface, was less apparent than the impact of the as-built grain structure. It can be argued that in the AB state the grain solidification and orientation has more effect on the crack propagation than the intrinsic mechanical properties difference between the dissimilar alloys IN718 and 316L. This could be explained further because, in the AB state, the IN718 does not display its full strength difference, as no thermal treatment was applied in order to allow the growth of its main strengthening secondary phase (γ‘ and γ’’). In addition the ductile behaviour of 316L fabricated by L-PBF in its AB state provides a high degree of toughness, which explains how 316L in the AB state can compete quite favourably with AB IN718 under cyclic testing. Hence the main discriminating factor between both alloys in the as-built case would be the structure of grain solidification (equiaxed for 316L and columnar for IN718) and the orientation of such grain structures with respect to the stress direction and direction of crack advance.

### 3.6. Multi-layer transition effect on crack propagation through 316L/IN718

*Bi-layer SENB specimen, growth at constant stress intensity factor*

In order to study this effect more fully, a crack propagation test was performed at constant ΔK through a bi-layer SENB specimen. In this test, the crack was initiated from the IN718 layer, and subjected to manual modification of the applied stress in order to keep the stress intensity at the crack tip constant (within ±10%) throughout the crack extension. The initial notch depth was a=1.3mm, then pre-cracking was performed by load shedding. The load was stepped down to a crack tip stress intensity factor of $\Delta K_{app}$=10.6 MPa√m, then was kept constant (within ±10%) for the rest of the experiment by adjusting the load iteratively, following the crack advance monitored by DCPD device. The starting crack depth including the pre-crack was $a_i$=1.99mm, and the test was conducted at R=0.1 and a frequency of 10Hz. The crack growth rate (da/dN) versus the crack depth is displayed in Figure 15, and the interface position is indicated by the red line.

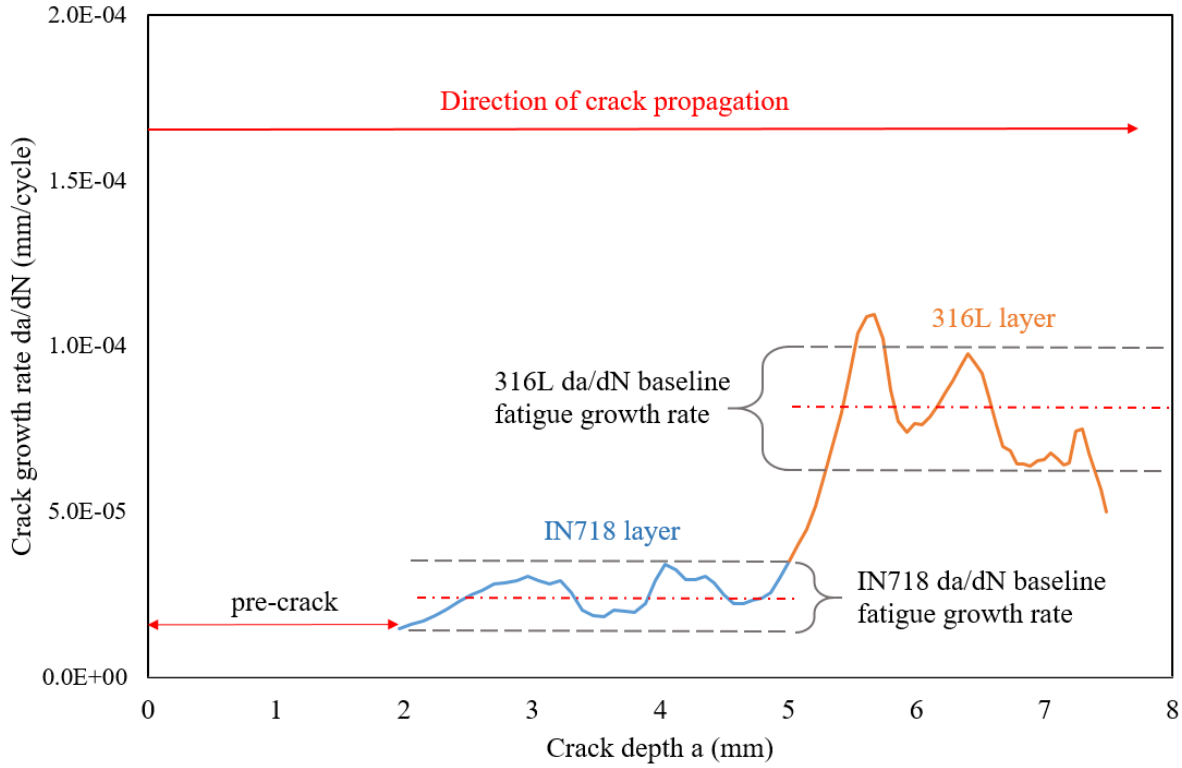


Figure 15: Crack growth rate versus crack tip depth, at ΔK=10.6MPa√m ±10%

Figure 15 shows that the crack growth rate is about $2.45\times 10^{-5} \pm 4.9 \times 10^{-6}$ mm/cycle within the IN718 layer then increased to $7.53\times 10^{-5} \pm 1.6 \times 10^{-5}$ mm/cycle within the 316L layer. An increase by a factor of three was noticed immediately after the interface transition, around 5 to 5.5 mm depth. A clear anti-shielding effect of the transition from harder IN718 into the softer more compliant 316L layer is visible here, it should be noted that no interface delamination was observed in the post-mortem fractography.

In order to incrementally extend the crack, the deformation and stresses at the crack tip need to overcome the local potential energy within a certain radius representative of the plastic zone

size ahead of the crack tip. Hence the definition of the necessary crack driving force for an incremental extension of the step size of the same radius. A given load will determine the radius of the pseudo-plastic zone ahead of the crack tip, for a given specimen geometry and material yield strength [44]. However, during the crack propagation through dissimilar material the yield stress follows a gradient that will cause changes in the local stress field, hence in the necessary potential energy to overcome for crack propagation. Local variation in the yield stress directly affects the near crack tip driving force. When the yield stress increases (in a transition gradient from soft to hard) the crack tip driving force is decreased, hence causing a crack propagation deceleration also known as a shielding effect [6].

It is important to recap the results from section 3.3, which showed that elastic properties were measured as continuous through the interface, only showing a difference in Yield stress and ductility. This allows the stress intensity assumption of similitude to hold, as long as the elastic properties remain continuous throughout the specimen [6]. The increase in strain energy increase required with regards to the distance of the crack tip from the interface, when the crack advances from a soft ($\sigma_{y1}$) to hard layer ($\sigma_{y2}$) ($\sigma_y$ having a negative gradient) has shown the decrease of the crack tip driving force can be up to 33% where $\sigma_{y2} = 2 * \sigma_{y1}$.

The radius of the plastic zone (Eq. 3) ahead of the crack tip for plane strain condition (in the centre of the specimen) can be calculated as follows [45]:

$$r_{pl} = \left(\frac{1}{6\pi}\right) \times \left(\frac{K_{max}}{\sigma_y}\right)^2 \propto (K/\sigma_y)^2 \quad (3)$$

At a constant ΔK value of 10.6MPa√m, the plastic zone ahead of the crack tip is about 0.32mm within the 316L region and about 0.24mm within the IN718 layer. If the interlayer thickness is larger than the radius of the plastic zone dimension, it will effectively affect the crack propagation. In our case the thickness of the 316L interlayer is three times larger than the radius of the plastic zone size, hence the yield stress difference should effectively shield the crack driving force when the plastic zone radius ahead of the crack tip is reaching the dissimilar materials interface.

Hence, the anti-shielding effect measured in our specimen was greater than expected and has showed a three fold increase in the crack propagation rate at a distance relatively close to the expected plastic zone size right after the dissimilar material interface (falling back to a lower level once the crack tip has progressed beyond the interface transitioning between the materials).

*4-layer SENB specimen*

Another fatigue crack growth experiment was conducted on a 4-layer specimen in AB condition under constant load range (increasing ΔK conditions). The crack propagation rates with increasing ΔK through the thickness of SENB specimen was recorded by DCPD again. Figure 16 shows that the notch is located in the IN718 top layer, a first pre-crack was obtained by load shedding until a depth of a = 2.16 mm and a starting ΔK of 12.3MPa√m.

The results of the crack propagation test through the multi-layer specimen is displayed in Figure 16. The crack was initiated in the IN718 layer, then propagated through the first interface IN718/316L (hard to soft) transition indicated by first red line on graph. After that,

the crack propagated through the 316L layer before reaching the second interface 316L/IN718 (from soft to hard), indicated by a red line on the graph. It can be seen that in the middle of the 316L layer, the crack propagation decreases and then reaches a plateau in growth rate, despite the increase in ΔK meaning that the crack is effectively slowed as it approaches the harder material and the crack tip experiences a positive yield stress gradient.

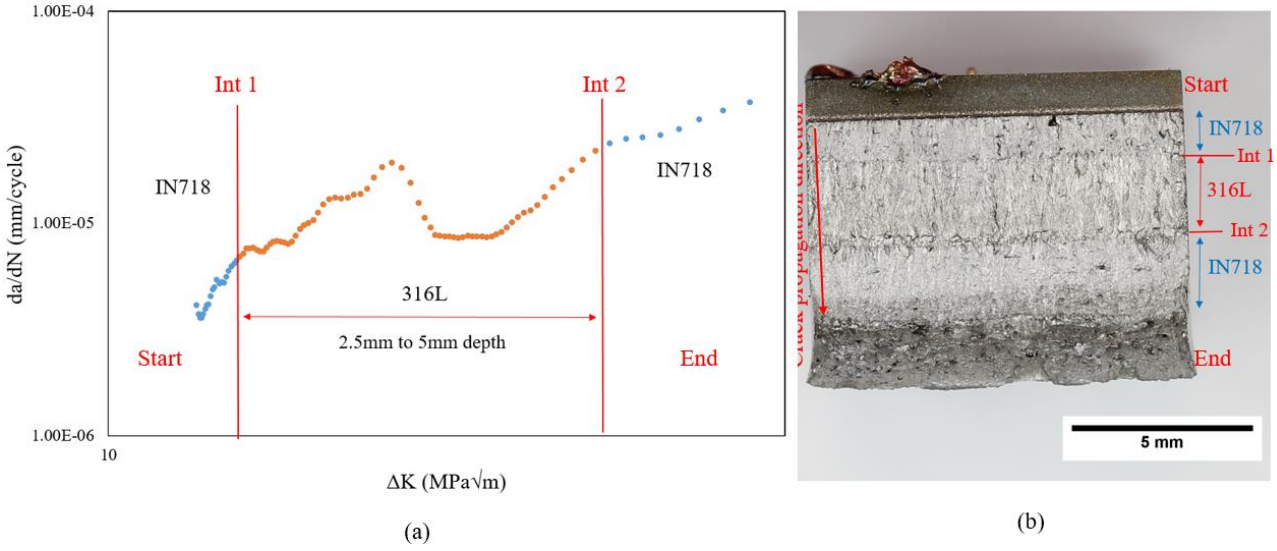


Figure 16 Crack propagation through multi-layer specimen, a) crack growth rate versus crack tip stress intensity factor, b) top view of final fracture surface

## 3.7. Fractography of 4-layered long crack specimen

The fracture surface of the 4-layer specimen has shown clearer mechanisms of crack shielding and anti-shielding in 316L/IN718 AB specimen. Due to the cellular nature of the grain structure in material fabricated by L-PBF, the local elemental segregation causes a fine network of weaker areas within grains. In the first IN718 layer (shown in Figure 17), where the crack growth was initiated, this cellular sub structure was encompassed by the crack propagation. Very fine striation spacing of < 1μm can be discriminated which is corresponding to the low initial crack propagation rate at a stress intensity factor range around <15 MPa√m. The spherical features observed within the IN718 layer are likely to be secondary phases such as carbides and Laves phases. The fracture surface remained overall flat and featureless showing a transgranular propagation with fine fatigue striations observed. This transgranular fatigue fracture surface is consistent with long crack test observations carried out on IN718 in the AB condition in the near threshold regime (with ΔK around 15 MPa√m, which corresponds to what was observed in section 3.4) from the literature [42].

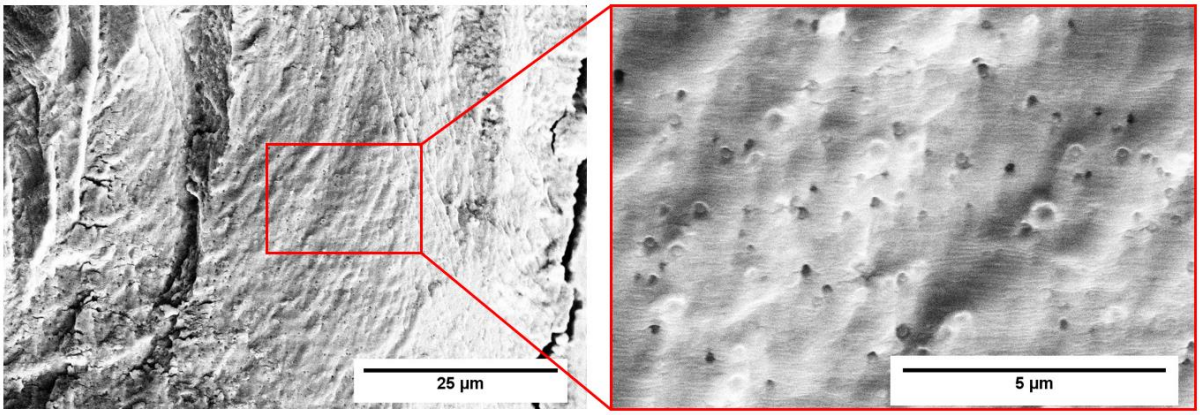


(a) (b)

Figure 17: SEM view of the top layer, crack initiation in IN718 layer

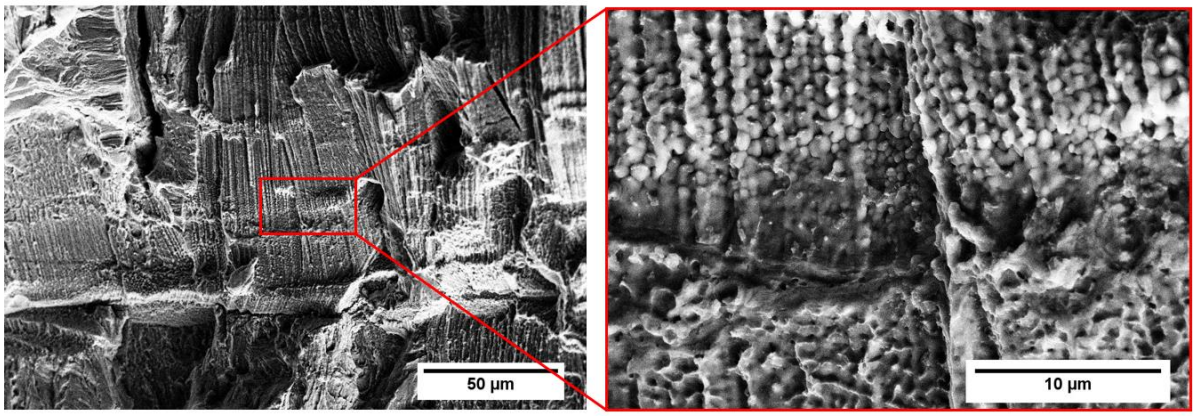


(a) (b)

Figure 18: SEM view of first interface

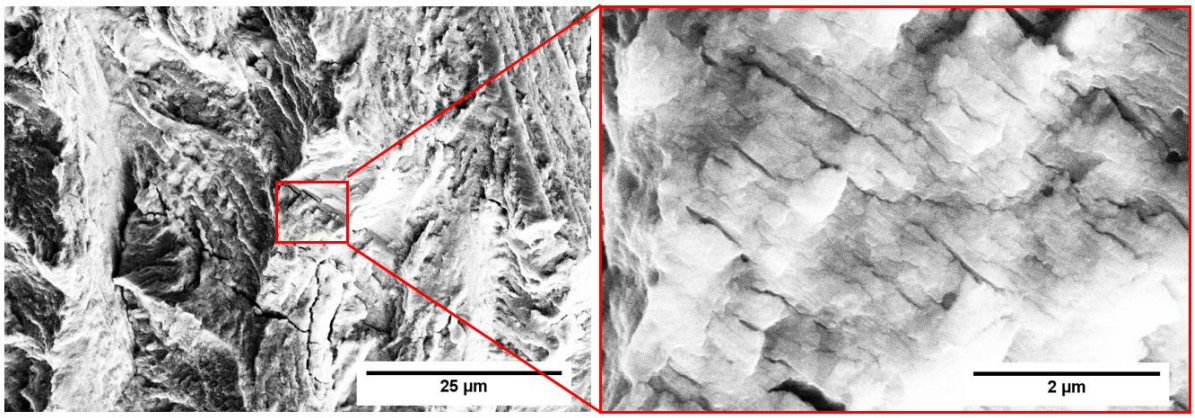


(a) (b)

Figure 19: SEM view of 316L layer (top of the layer)

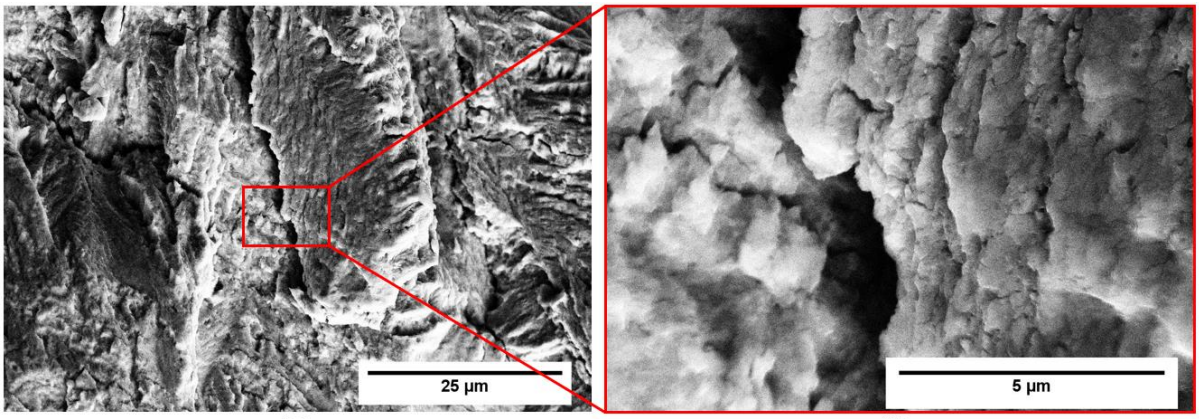


(a) (b)

Figure 20: SEM view of 316L layer (bottom before the second interface)

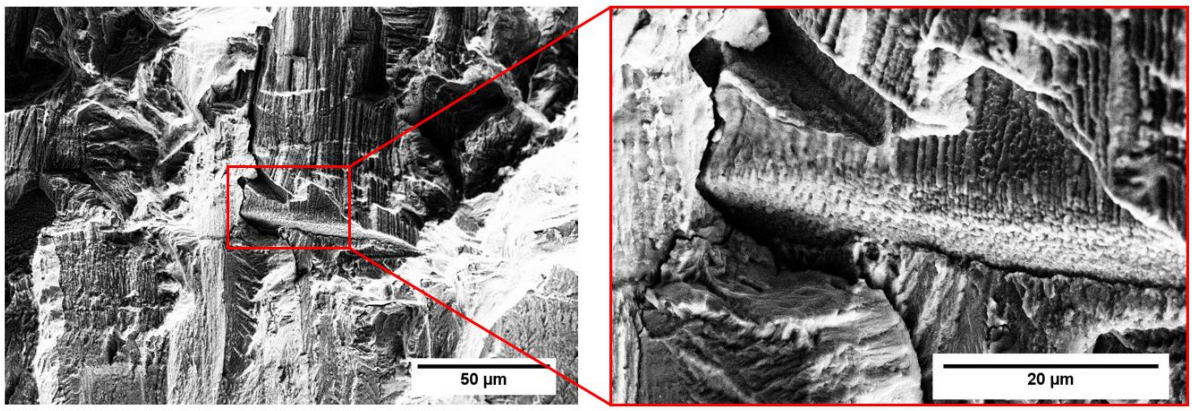


(a) (b)

Figure 21: SEM view of the second interface

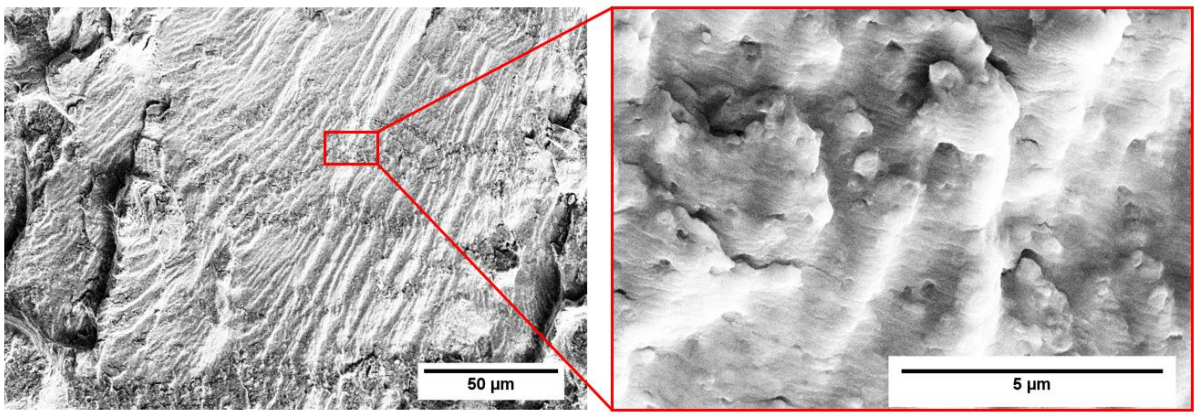


(a) (b)

Figure 22: SEM view of the IN718 bottom layer

In Figure 18 the first interface shows a clear interdendritic decohesion fatigue mechanism that is considered to be due to the stronger effect of partitioning around the interface. Within the dendrite the gradual solidification causes the core of the dendrite to first solidify as γ matrix, then an eutectic layer of γ/γ', and an outer layer of the last solidified elements segregate such as Nb which is one of the most sluggish to react with Nickel, or carbides. At the interface the elemental concentration of Iron is inferred from the local partitioning of Niobium, that has an

even lower solubility in Iron than in Nickel, hence supporting a stronger partitioning effect in this area [46].

Figure 19 and Figure 20 are both SEM views of fatigue propagation in the 316L interlayer. Figure 19 shows the fracture surface for $\Delta K$ of 14 MPa$\sqrt{m}$ and for a growth rate da/dN of $8.10^{-6}$ mm/cycle while Figure 20 shows the fracture surface for $\Delta K$ of 26 MPa$\sqrt{m}$, and a growth rate around $1.10^{-5}$ mm/cycle While both areas of the fracture surface show an overall rougher macro-texture, the presence of secondary cracks around the cellular sub-structure was observed. It can be seen that the secondary cracks are more widely opened at the bottom of the layer, just before the second interface transition (which occurs at higher $\Delta K$ levels around 30MPa$\sqrt{m}$). Due to the difference in yield strength and ductility levels between 316L and IN718 it is expected to see a shielding effect of the crack propagation around (just before) the second interface. A stabilisation in the crack propagation rate was measured around 0.5 mm before the second interface, and the fractography revealed the presence of multiple secondary cracks that show significant opening throughout the 316L microstructure in this area. The release of energy via the local opening and widening of the secondary cracks surrounding the cellular sub-structure within the 316L layer is causing additional shielding effects in this area.

In Figure 21 a visible interdendritic decohesion was observed at the second interface, and a similar transgranular crack propagation was captured in the bottom IN718 layer, see Figure 22. Some secondary cracks appear as well in this layer due to the increase in stress intensity factor range, from 30 to 60 MPa$\sqrt{m}$, that is represented by the final fast growth of the crack propagation, up to $5.10^{-5}$mm/cycle on the graph shown in Figure 16, which in that area is approaching final monotonic failure of the specimen .

## 4. Conclusions

The present work shows the clear effect of the microstructure, and varying mechanical properties of 316L and IN718 alloys built by MMAM in their AB state, on the fatigue behaviour of layered specimens. The main results are summarised as follows:

- Solidification of 316L and IN718 was observed to create very different grain structures, a columnar grain growth was observed in IN718 and an equiaxed grain structure in the 316L region.
- The mechanical properties of 316L and IN718 in AB state show similar elastic response, while showing a more pronounced difference in plastic properties, most importantly in the % elongation under plastic deformation (and a more modest difference in yield strengths).
- The crack propagation rate was measured through bi-layer specimens under increasing $\Delta K$ conditions and it was observed that the grain structure and orientation most strongly affect the crack propagation rate, particularly at lower $\Delta K$ levels.
- A transgranular crack growth mode was observed through the IN718 layer compared to a mix of transgranular and intergranular more tortuous crack paths taken within the 316L layer
- A clear inter-dendritic decohesion was observed at the dissimilar material interface showing a stronger effect of elemental partitioning at the interface, weakening the interdendritic areas
- The crack propagation through the 4-layer specimen has showed a shielding effect of the crack propagation just before the transition from the soft 316L layer to the hard IN718 layer
- The shielding of the crack propagation process was linked to the apparent release of energy by the opening and widening of secondary cracks within the 316L interlayer.

## 5. Acknowledgements

This study was made possible thanks to the Centre for Doctoral Training in Sustainable Infrastructure System (CDT-SIS) funded by the Engineering and Physical Sciences Research Council (EPSRC) and the National Structural Integrity Research Centre (NSIRC), by funding this PhD program hosted by both the University of Southampton and The Welding Institute (TWI) of Cambridge. The associated grant reference is the EP/L01582X/1. M-S D-C is grateful for funding from the Lloyd's Register Foundation, a charitable foundation helping protect life and property by supporting engineering-related education, public engagement, and the application of research.

## 6. References

[1] A. Busachi, J. Erkoyuncu, P. Colegrove, F. Martina, C. Watts, and R. Drake, "A review of Additive Manufacturing technology and Cost Estimation techniques for the defence sector," *CIRP J. Manuf. Sci. Technol.*, vol. 19, pp. 117–128, 2017.

[2] M. Vaezi, S. Chianrabutra, B. Mellor, and S. Yang, "Multiple material additive manufacturing - Part 1: A review: This review paper covers a decade of research on multiple material additive manufacturing

technologies which can produce complex geometry parts with different materials," *Virtual Phys. Prototyp.*, vol. 8, no. 1, pp. 19–50, 2013.
[3] M. Naebe and K. Shirvanimoghaddam, "Functionally graded materials: A review of fabrication and properties," *Appl. Mater. Today*, vol. 5, pp. 223–245, 2016.
[4] B. E. Carroll *et al.*, "Acta Materialia Functionally graded material of 304L stainless steel and inconel 625 fabricated by directed energy deposition : Characterization and thermodynamic modeling," *Acta Mater.*, vol. 108, pp. 46–54, 2016.
[5] A. Hinojos *et al.*, "Joining of Inconel 718 and 316 Stainless Steel using electron beam melting additive manufacturing technology," *Mater. Des.*, vol. 94, pp. 17–27, 2016.
[6] O. Kolednik, "The yield stress gradient e ect in inhomogeneous materials," vol. 37, pp. 781–808, 2000.
[7] S. Mohd Yusuf, M. Nie, Y. Chen, S. Yang, and N. Gao, "Microstructure and corrosion performance of 316L stainless steel fabricated by Selective Laser Melting and processed through high-pressure torsion," *J. Alloys Compd.*, vol. 763, pp. 360–375, 2018.
[8] E. Chlebus, K. Gruber, B. Ku, J. Kurzac, and T. Kurzynowski, "Materials Science & Engineering A Effect of heat treatment on the microstructure and mechanical prop- erties of Inconel 718 processed by selective laser melting," vol. 639, pp. 647–655, 2015.
[9] I. Tolosa, F. Garciandía, F. Zubiri, F. Zapirain, and A. Esnaola, "Study of mechanical properties of AISI 316 stainless steel processed by 'selective laser melting', following different manufacturing strategies," *Int. J. Adv. Manuf. Technol.*, vol. 51, no. 5–8, pp. 639–647, 2010.
[10] T. Trosch, J. Strößner, R. Völkl, and U. Glatzel, "Microstructure and mechanical properties of selective laser melted Inconel 718 compared to forging and casting," *Mater. Lett.*, vol. 164, pp. 428–431, 2016.
[11] S. J. Zinkle and G. S. Was, "Materials challenges in nuclear energy," *Acta Mater.*, vol. 61, no. 3, pp. 735–758, 2013.
[12] C. Wei and E. T. Al, "Multiple -material selective laser melting: a new approach" no. 89, pp. 18–19, 2018.
[13] O. Kolednik, J. Zechner, and J. Predan, "Scripta Materialia Improvement of fatigue life by compliant and soft interlayers," *SMM*, vol. 113, pp. 1–5, 2016.
[14] W. J. Sames, F. A. List, S. Pannala, R. R. Dehoff, and S. S. Babu, "The metallurgy and processing science of metal additive manufacturing," *Int. Mater. Rev.*, vol. 61, no. 5, pp. 315–360, 2016.
[15] H. D. Carlton, A. Haboub, G. F. Gallegos, D. Y. Parkinson, and A. A. Macdowell, "Materials Science & Engineering A Damage evolution and failure mechanisms in additively manufactured stainless steel," *Mater. Sci. Eng. A*, vol. 651, pp. 406–414, 2016.
[16] D. Wang, C. Song, Y. Yang, and Y. Bai, "Investigation of crystal growth mechanism during selective laser melting and mechanical property characterization of 316L stainless steel parts," *Mater. Des.*, vol. 100, pp. 291–299, 2016.
[17] P. Petrzak, K. Kowalski, and M. Blicharski, "Analysis of Phase Transformations in Inconel 625 Alloy during Annealing," vol. 130, no. 4, 2016.
[18] W. M. Tucho, P. Cuvillier, A. Sjolyst-kverneland, and V. Hansen, "Materials Science & Engineering A Microstructure and hardness studies of Inconel 718 manufactured by selective laser melting before and after solution heat treatment," *Mater. Sci. Eng. A*, vol. 689, no. February, pp. 220–232, 2017.
[19] Y. M. Wang *et al.*, "Additively manufactured hierarchical stainless steels with high strength and ductility," *Nat. Mater.*, vol. 17, no. 1, pp. 63–70, 2018.
[20] Y. Zhong, L. Liu, S. Wikman, D. Cui, and Z. Shen, "Intragranular cellular segregation network structure strengthening 316L stainless steel prepared by selective laser melting," *J. Nucl. Mater.*, vol. 470, pp. 170–178, 2016.
[21] J. Suryawanshi, K. G. Prashanth, and U. Ramamurty, "Mechanical behavior of selective laser melted 316L stainless steel," *Mater. Sci. Eng. A*, vol. 696, no. April, pp. 113–121, 2017.
[22] K. Saeidi, X. Gao, Y. Zhong, and Z. J. Shen, "Hardened austenite steel with columnar sub-grain structure formed by laser melting," *Mater. Sci. Eng. A*, vol. 625, pp. 221–229, 2015.
[23] "ASTM B213-20 Standard Test Methods for Flow Rate of metal Powders Using the Hall Flowmeter Funnel," *ASTM Int.*, 2020.
[24] S. M. Yusuf and N. Gao, "Influence of energy density on metallurgy and properties in metal additive manufacturing," *Mater. Sci. Technol.*, vol. 33, no. 11, pp. 1269–1289, 2017.
[25] M. Ni, C. Chen, X. Wang, P. Wang, R. Li, and X. Zhang, "Materials Science & Engineering A Anisotropic tensile behavior of in situ precipitation strengthened Inconel 718 fabricated by additive manufacturing," *Mater. Sci. Eng. A*, vol. 701, no. June, pp. 344–351, 2017.

[26] T. Peng and C. Chen, “Influence of energy density on energy demand and porosity of 316L stainless steel fabricated by selective laser melting,” *Int. J. Precis. Eng. Manuf. Technol.*, vol. 5, no. 1, pp. 55–62, 2018.
[27] 6507, “Metallic materials. Vickers hardness test. Test method,” *BS EN ISO*, 2018.
[28] A. E8/E8M, “16ae1 Standard test Methods for Tension Testing of Metallic Materials,” *ASTM Int.*
[29] BSI, “BSI Standards Publication Metallic materials — Fatigue testing — Fatigue crack growth method,” 2012.
[30] M. S. Pham, B. Dovgyy, and P. A. Hooper, “Twinning induced plasticity in austenitic stainless steel 316L made by additive manufacturing,” *Mater. Sci. Eng. A*, vol. 704, no. April, pp. 102–111, 2017.
[31] M. Lecture-iron and S. Division, “Solidification Processing,” 1974.
[32] Z. W. Chen, M. A. L. Phan, and K. Darvish, “Grain growth during selective laser melting of a Co – Cr – Mo alloy,” *J. Mater. Sci.*, vol. 52, no. 12, pp. 7415–7427, 2017.
[33] G. Posch, R. Vallant, W. Klagges, and H. Cerjak, “Influence of Niobium on mechanical properties and hot crack susceptibility of Nickel-base cored-wire weld metal type 70 / 20 and 70 / 15 Cracking in Nickelbasis-weldments Solidification cracking,” vol. 2000, 2000.
[34] R. Saluja, “The emphasis of the phase transformations and alloying constituants on hot cracking susceptibility of type 304L and 316L stainless steel welds,” vol. 4, no. 05, pp. 2206–2216, 2012.
[35] C. Wei, L. Li, X. Zhang, and Y. H. Chueh, “3D printing of multiple metallic materials via modified selective laser melting,” *CIRP Ann.*, vol. 67, no. 1, pp. 245–248, 2018.
[36] F. Liu *et al.*, “The effect of laser scanning path on microstructures and mechanical properties of laser solid formed nickel-base superalloy Inconel 718,” *J. Alloys Compd.*, vol. 509, no. 13, pp. 4505–4509, 2011.
[37] Z. Jones, K. Cooper, and K. Chou, “MSEC2015-9317,” no. January 2015, 2017.
[38] S. Uns and S. W. Nr, “Specification Sheet : Alloy 316 / 316L,” no. 1, pp. 9–11, 2014.
[39] AMS5383, “Nickel Alloy, Corrosion and Heat-Resistant, Investment Casting, 52.5Ni-19Cr-3.0Mo-5.1Cb(Nb)-0.9Ti-0.6Al-18Fe, Vacuum Melted Homogenization and Solution Heat Treated,” *SAE Int.*
[40] M. S. Pham, C. Solenthaler, K. G. F. Janssens, and S. R. Holdsworth, “Dislocation structure evolution and its effects on cyclic deformation response of AISI 316L stainless steel,” *Mater. Sci. Eng. A*, vol. 528, no. 7–8, pp. 3261–3269, 2011.
[41] J. Zechner and O. Kolednik, “Fracture resistance of aluminum multilayer composites,” *Eng. Fract. Mech.*, vol. 110, pp. 489–500, 2013.
[42] L. Kunz, G. Nicoletto, and A. Bac, “Long fatigue crack growth in Inconel 718 produced by selective laser melting,” vol. 92, pp. 499–506, 2016.
[43] A. Riemer, S. Leuders, M. Thöne, H. A. Richard, T. Tröster, and T. Niendorf, “On the fatigue crack growth behavior in 316L stainless steel manufactured by selective laser melting,” *Eng. Fract. Mech.*, vol. 120, pp. 15–25, 2014.
[44] U. Krupp, *Fatigue Crack Propagation in Metals and Alloys*. .
[45] Y. Sugimura and P. G. Lim, “Fracture normal to a bimaterial interface: effect of plasticity on crack-top shielding and amplification,” vol. 43, no. 3, pp. 1157–1169, 1995.
[46] S. D. K. John N Dupont, John CLippold, *Welding Metallurgy and Weldalitity of Nickel-base alloys*. 2009.